Ultramicroscopy 171 (2016) 55–62

Contents lists available at ScienceDirect

Ultramicroscopy

journal homepage: www.elsevier.com/locate/ultramic

Three dimensional mapping of Fe dopants in ceria nanocrystals using direct spectroscopic electron tomography

Bart Goris [a], Maria Meledina [a], Stuart Turner [a], Zhichao Zhong [b], K. Joost Batenburg [b,c], Sara Bals [a,*]

[a] EMAT, University of Antwerp, Groenenborgerlaan 171, 2020 Antwerp, Belgium
[b] Centrum Wiskunde & Informatica, P.O. Box 94079, 1090 GB Amsterdam, The Netherlands
[c] Mathematical Institute, Leiden University, Niels Bohrweg 1, 2333CA Leiden, The Netherlands

ARTICLE INFO

Article history:
Received 20 May 2016
Received in revised form
22 August 2016
Accepted 29 August 2016
Available online 30 August 2016

Keywords:
Electron tomography
EELS
Spectroscopy
Ceria nanoparticles
Dopants
Valency

ABSTRACT

Electron tomography is a powerful technique for the 3D characterization of the morphology of nanostructures. Nevertheless, resolving the chemical composition of complex nanostructures in 3D remains challenging and the number of studies in which electron energy loss spectroscopy (EELS) is combined with tomography is limited. During the last decade, dedicated reconstruction algorithms have been developed for HAADF-STEM tomography using prior knowledge about the investigated sample. Here, we will use the prior knowledge that the experimental spectrum of each reconstructed voxel is a linear combination of a well-known set of references spectra in a so-called direct spectroscopic tomography technique. Based on a simulation experiment, it is shown that this technique provides superior results in comparison to conventional reconstruction methods for spectroscopic data, especially for spectrum images containing a relatively low signal to noise ratio. Next, this technique is used to investigate the spatial distribution of Fe dopants in Fe:Ceria nanoparticles in 3D. It is shown that the presence of the Fe^{2+} dopants is correlated with a reduction of the Ce atoms from Ce^{4+} towards Ce^{3+}. In addition, it is demonstrated that most of the Fe dopants are located near the voids inside the nanoparticle.

1. Introduction

A three-dimensional (3D) characterization of the morphology of nanostructures can nowadays routinely be obtained using electron tomography. This technique combines a tilt series of two-dimensional (2D) projection images into a 3D reconstruction using a mathematical algorithm [1]. Currently, most results in materials science are obtained using high angle annular dark field (HAADF) scanning transmission electron microscopy (STEM). HAADF-STEM fulfils the projection requirement for electron tomography, since the contribution of diffraction contrast in the resulting projection images is reduced and, up to a certain thickness, the intensity scales linearly with thickness [2]. In addition, chemical information can be obtained because the projected intensity is proportional to the integrated atomic weight of the specimen. Nevertheless, it is not straightforward to interpret the grey levels in a 3D HAADF-STEM reconstruction in an absolute manner. Therefore, it is challenging to use HAADF-STEM tomography for samples in which mixing of elements is expected. Also for samples that contain unknown elements or elements with atomic number Z close to each other, obtaining 3D chemical information by HAADF-STEM tomography is certainly not straightforward. This problem can be overcome by using spectroscopic techniques such as energy dispersive X-ray imaging (EDX) or electron energy loss spectroscopy (EELS). In the past, electron tomography in combination with EELS imaging techniques was applied to investigate nanostructures in both materials science and biology [3–8]. In most studies, 2D elemental maps of the object are first calculated at each tilt angle and used as an input for tomographic reconstruction. These 2D elemental maps are obtained through a background subtraction and a summation over several energy levels or using more dedicated techniques such as multivariate analysis (MVA) or spectrum fitting [9–11]. However, in this manner, part of the EELS spectrum is omitted and systematic errors may accumulate in the final reconstruction. An alternative is to reconstruct each energy loss separately yielding a 4D data cube where an EELS spectrum can be extracted from each 3D voxel. This method was for example recently used for the characterization of an Al–5 wt% Si alloy and for the 3D investigation of variations of the valence state of Ce in ceria nanocrystals [3,12].

During the last decade, specialized reconstruction algorithms that use prior knowledge on the investigated sample have been developed [13–15]. For example, the discrete algebraic

* Corresponding author.

http://dx.doi.org/10.1016/j.ultramic.2016.08.017
0304-3991/

reconstruction technique (DART) is based on the idea that a 3D HAADF-STEM reconstruction of a (nano)material only contains a limited number of grey values [13]. In this manner, several artefacts, typical to electron tomography, are minimized yielding reconstructions with a higher reliability. An additional advantage of discrete tomography is that the quantification of the final reconstruction is straightforward since the segmentation is part of the reconstruction algorithm. Here, we will exploit the prior knowledge that a sample is constituted from a limited number of well-known components to spectroscopic data. By using direct spectroscopic electron tomography, fitting of reference spectra of the different chemical components is combined with the tomographic reconstruction in a single step. Using this approach, the intermediate step where 2D elemental maps are first extracted from the projected spectrum images prior to the tomographic reconstruction is omitted. Consequently, the large errors that may accumulate, especially when a low signal to noise ratio (SNR) is present in the projection data, are reduced by combining information from all different tilt angles directly during the reconstruction. This approach enables us to improve the quality of 3D reconstructions when a low SNR is present in the projection data.

Here, we apply direct spectroscopic electron tomography to investigate the presence and location of small Fe dopants in Fe: ceria nanocrystals. The investigation of dopants in small nanoparticles is an excellent example of a study in which STEM-EELS spectrum images with a low SNR can be expected. The samples were synthesized by co-precipitation of nitrates followed by a thermal treatment [16,17]. This synthesis results in ceria nanoparticles with a truncated octahedral morphology and rich in faceted voids. In previous work, 2D EELS mapping was used to evidence that the Fe dopants aggregate mainly at the outer Ce surface and the walls of the voids [17]. Here, we will investigate the correlation between the location of the Fe dopants and changes in the valency of the Ce nanoparticle in 3D in more detail. This type of information cannot be retrieved in a straightforward manner from single 2D projections because of the limited SNR and the projective nature of the experimental data.

2. Direct spectroscopic electron tomography

During an EELS tomography experiment, an EELS data cube is acquired at each tilt angle. The vector $\boldsymbol{p}^{(i)}$ represents all projected intensities in a tilt series for the i^{th} energy channel. Therefore, a complete spectroscopic tomography experiment yields a set of $\{\boldsymbol{p}^{(1)}, \boldsymbol{p}^{(2)},\ldots,\boldsymbol{p}^{(l)}\}$ different tilt series where l represents the number of different energy channels. Mathematically, the reconstruction $\boldsymbol{x}^{(i)}$ of the i^{th} energy loss can be understood as an individual reconstruction problem described by the following set of linear equations:

$$\boldsymbol{p}^{(i)} = W\boldsymbol{x}^{(i)}$$

Here, the matrix W is the tomographic projection matrix describing the contribution of each 3D voxel to all projected intensities. A reconstruction of all energy levels separately then corresponds to solving the combined set of linear equations:

$$\begin{bmatrix} \boldsymbol{p}^{(1)} \\ \boldsymbol{p}^{(2)} \\ \vdots \\ \boldsymbol{p}^{(l)} \end{bmatrix} = \begin{bmatrix} W & 0 & \ldots & 0 \\ 0 & W & \ldots & \vdots \\ \vdots & \vdots & \ddots & 0 \\ 0 & \ldots & 0 & W \end{bmatrix} \begin{bmatrix} \boldsymbol{x}^{(1)} \\ \boldsymbol{x}^{(2)} \\ \vdots \\ \boldsymbol{x}^{(l)} \end{bmatrix}$$

One can now use the prior knowledge that the resulting EELS spectrum at each voxel consists of m different chemical components. The distribution of a chemical component j is represented by a vector $\boldsymbol{e}_j$ that corresponds to a voxel volume for that particular element. The corresponding reference spectrum is provided by $\left\{ r_j^{(1)}, r_j^{(2)},\ldots,r_j^{(l)} \right\}$. Mathematically, this can be formulated as the following matrix multiplication:

$$\begin{bmatrix} \boldsymbol{x}^{(1)} \\ \boldsymbol{x}^{(2)} \\ \vdots \\ \boldsymbol{x}^{(l)} \end{bmatrix} = \begin{bmatrix} r_1^{(1)} & r_2^{(1)} & \ldots & r_m^{(1)} \\ r_1^{(2)} & r_2^{(2)} & \ldots & r_m^{(2)} \\ \vdots & \vdots & \ddots & \vdots \\ r_1^{(l)} & r_2^{(l)} & \ldots & r_m^{(l)} \end{bmatrix} \begin{bmatrix} \boldsymbol{e}_1 \\ \boldsymbol{e}_2 \\ \vdots \\ \boldsymbol{e}_m \end{bmatrix}$$

Combining this information with the reconstruction problem provides us the following set of linear equations:

$$\begin{bmatrix} \boldsymbol{p}^{(1)} \\ \boldsymbol{p}^{(2)} \\ \vdots \\ \boldsymbol{p}^{(l)} \end{bmatrix} = \begin{bmatrix} W & 0 & \ldots & 0 \\ 0 & W & \ldots & \vdots \\ \vdots & \vdots & \ddots & 0 \\ 0 & \ldots & 0 & W \end{bmatrix} \begin{bmatrix} r_1^{(1)} & r_2^{(1)} & \ldots & r_m^{(1)} \\ r_1^{(2)} & r_2^{(2)} & \ldots & r_m^{(2)} \\ \vdots & \vdots & \ddots & \vdots \\ r_1^{(l)} & r_2^{(l)} & \ldots & r_m^{(l)} \end{bmatrix} \begin{bmatrix} \boldsymbol{e}_1 \\ \boldsymbol{e}_2 \\ \vdots \\ \boldsymbol{e}_m \end{bmatrix}$$

This can be solved using conventional tomographic reconstruction techniques such as the simultaneous iterative reconstruction technique (SIRT) [18]. In addition, different types of prior knowledge about the spatial extent of the different chemical contributions can be incorporated, using more dedicated reconstruction techniques such as a compressive sensing based reconstruction technique or discrete tomography [13–15]. Because the number of chemical components is typically much smaller than the number of energy channels ($m \ll l$), the number of unknown variables in the reconstruction problem is drastically reduced, whereas the number of projection intensities remains constant, yielding a significant improvement in the quality of the final reconstructions. A flowchart comparing direct spectroscopic electron tomography to two conventional methods that have been used previously is presented in Fig. 1. In the first conventional method, individual elemental maps are extracted from the acquired spectrum images at each tilt angle by fitting reference spectra to the data. Next, these elemental maps are used as an input for a tomographic reconstruction. In the second method, all energy levels are reconstructed individually and the reference spectra are fitted afterwards to these reconstructions yielding a reconstruction of the individual elements. The third method corresponds to the method that we propose here in which prior knowledge about the reference spectra is combined with the tomographic reconstruction in a single step.

It must be noted that for the reconstruction of a 2D slice with size $(n \times n)$ using l different tilt angles, the tomographic projection operator is increased from size $(n.\ l{\times}n^2)$ to $(n.\ l.\ k{\times}n^2.\ k)$ where k equals the number of energy losses. Typically, this enlarges the tomography problem with a factor of several thousands, hampering the use of explicit projection matrices because of memory problems. To overcome these limitations, the ASTRA toolbox was used in combination with SPOT operators [19–21]. Such operators are mathematical objects that represent a matrix without the need to explicitly save all the elements. Furthermore, the operators can be used for calculations in a straightforward manner, enabling them to be used in the ASTRA toolbox without altering the existing tomographic reconstruction algorithms.

3. Phantom study

To investigate the performance of direct spectroscopic electron tomography, a phantom object resembling a Ce nanoparticle was simulated. The outer surface of ceria nanoparticles is usually

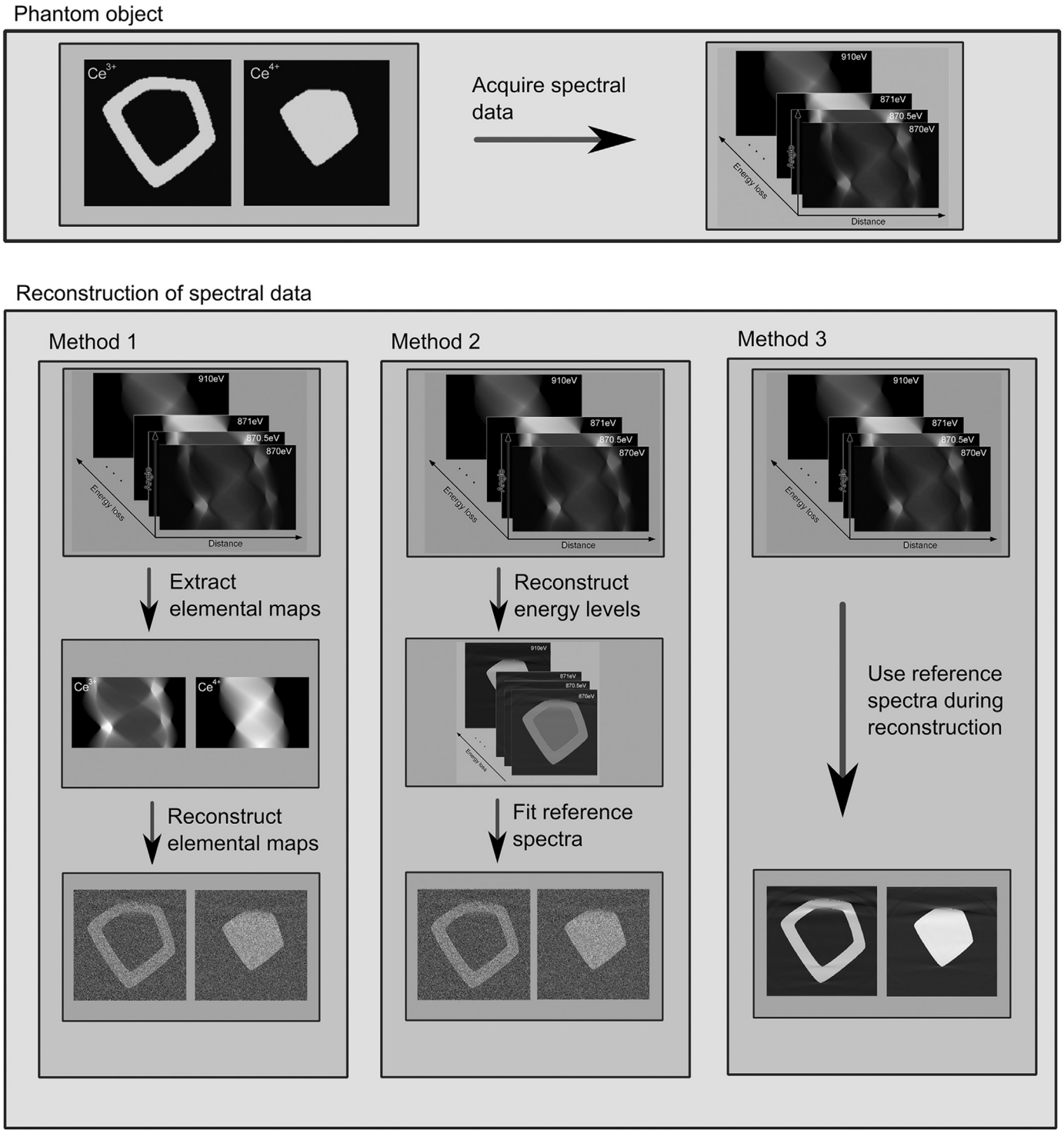

Fig. 1. Flowchart of spectroscopic electron tomography experiment. For the reconstruction of a 2D slice containing two different elements, three different methods for the reconstruction are displayed. In the first method, the sinograms of the individual elemental maps are first extracted and then reconstructed. The second method first reconstructs each energy channel separately and then uses the reference spectra to obtain the reconstructions of the elemental maps. In the third method, a novel reconstruction technique is applied where the fitting of the reference spectra is applied during the reconstruction.

reduced from Ce^{4+} to Ce^{3+} by the creation of oxygen vacancies, as shown previously by both 2D and 3D EELS mapping [3,22]. In addition, it is known that the surface morphology mostly corresponds to an octahedron that is composed of eight different {111} facets whereas a small truncation at the {001} facets may be present. Visualizations of the phantom object are presented in Fig. 2a. Projection images were simulated for different cases where both the tilt range and the tilt increment are altered. In addition, Poisson noise was added to the projection data yielding datasets with different SNR.

The simulated datasets are used as an input for the three different reconstruction approaches that were discussed previously and the results are summarized in Fig. 2b–d. For each approach, the tomographic reconstructions were calculated using a simultaneous iterative reconstruction technique (SIRT) with 100 iterations. Fig. 2b–d show the average reconstruction error defined

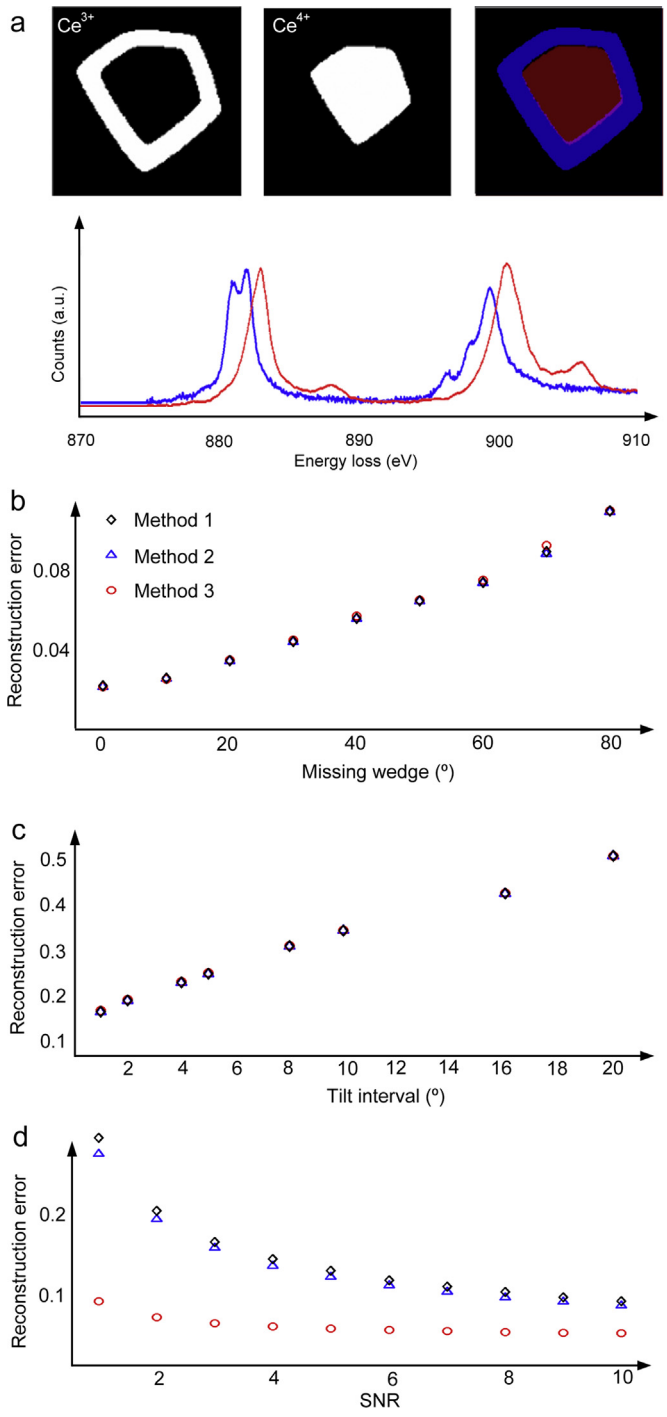

Fig. 2. (a) Phantom object containing 2 different chemical compositions. The reference spectra for Ce^{4+} and Ce^{3+} are displayed in red and blue respectively. For this phantom object, a spectroscopic tilt series is simulated and reconstructed using the three different methods explained in Fig. 1. (b) Average reconstruction error as a function of missing wedge. For an increasing missing wedge, the reconstruction error increases for all three methods. (c) Average reconstruction error as a function of tilt interval. (d) Average reconstruction error as a function of SNR in the projections. For a low SNR, a better reconstruction is obtained using method 3.

as the absolute difference between the reconstruction and the phantom object divided by the number of pixels. From Fig. 2b and c, it can be observed that for noise-free datasets, all reconstruction techniques provide comparable results, even when a missing wedge or a large tilt increment is present. However, Fig. 2d indicates that the direct reconstruction approach provides superior results when more noise is added to the datasets. This can be understood because the first two methods contain two different steps: fitting of reference spectra and tomographic reconstructions. Because of the presence of noise in the projection data, both of these processes introduce errors which will accumulate in the final reconstruction. The accumulation of artefacts is avoided using the approach that we present here since fitting and tomographic reconstruction are performed simultaneously, thereby integrating all available information for each of the compositions and for all tilt angles in the fitting steps.

4. Experimental results and discussion

The previous phantom study indicates that the direct reconstruction approach yields an improved reconstruction when a low SNR is present in the acquired tilt series of spectrum images. STEM-EELS data with a low SNR is common when investigating small dopants inside larger nanoparticles. Here, we investigate the presence of Fe dopants in the Fe:Ceria nanoparticles using a combination of HAADF-STEM imaging and EELS spectroscopy. The data was acquired using an aberration corrected cubed FEI Titan microscope operated at 120 kV. The monochromator was excited yielding an energy resolution of 300 meV. The energy resolution was measured using the full width half maximum of the zero-loss peak. The convergence semi-angle α used for the experiments was 18 mrad, the acceptance semi-angle for EELS and the inner HAADF-STEM detection angle were 61 mrad. A HAADF-STEM projection image of the investigated CeO_2 nanoparticle is presented in Fig. 3a. A accumulated EELS spectrum over the entire nanoparticle is presented in Fig. 3b, and the Fe $L_{2,3}$ and the Ce M_5 edges are marked. When inspecting the summed EELS spectrum, the low SNR is prevalent, hampering a straightforward extraction of the valency of the Fe dopants. The dark features in the HAADF-STEM projection image are related to the presence of small voids inside the nanocrystal as shown previously by Meledina et al. [17].

In order to investigate the spatial distribution of Fe in more detail, high resolution STEM-EELS experiments were acquired as presented in Fig. 4. These results indicate that most of the Fe dopants are present close to the voids within the ceria nanocrystals. In addition, it was shown previously that an increased concentration of Fe is found on the surface of the nanoparticles [17]. When inspecting the fine structure of the Fe $L_{2,3}$ edge in the EELS spectrum as presented in Fig. 4b, it is clear that the spectrum suggest the presence of mainly Fe^{2+}. This is clear from the inset of Fig. 4b where the experimental spectrum (blue) is compared to reference spectra of Fe^{2+} (red) and Fe^{3+} (green).

The results already provide some preliminary information on the investigated Ce nanoparticles, but it should be stressed that the spectra are based on 2D projections of a 3D object. It is therefore difficult to determine the valency of the Ce nanoparticle at the locations where the Fe dopants are present because of the projective nature of the data. In order to obtain this kind of information, a complete 3D characterization is required using spectroscopic electron tomography.

We therefore used a complete tilt series of EELS datacubes as an input for our reconstruction approach. The data was acquired using tilt angles ranging from $-70°$ to $+65°$ with a 5° tilt increment. The pixel size of the EELS datacube was 0.81 nm and an energy dispersion of 0.1 eV was used. In order to reduce the background signal, a nanoparticle (Fig. 3a) located above a vacuum region of the support grid was selected. The size of the nanoparticle was approximately 20 nm which guarantees that multiple scattering effects can be ignored during the reconstruction. Prior to using the EELS datacubes for the reconstruction, both spatial and energy drift needs to be corrected. The spatial drift parameters were found using a least square fitting of the slow scanned EELS

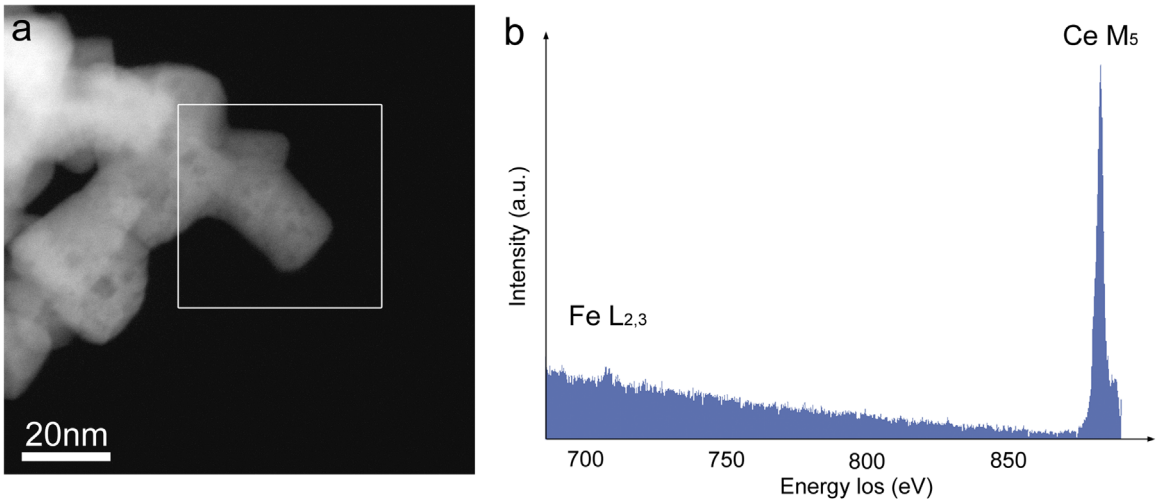

Fig. 3. STEM-EELS measurements of Fe doped ceria nanoparticle. (a) 2D projection image of Fe doped ceria nanoparticle at 0° tilt angle. (b) EELS spectrum of the nanoparticle accumulated over the region as indicated in (a) showing a low SNR.

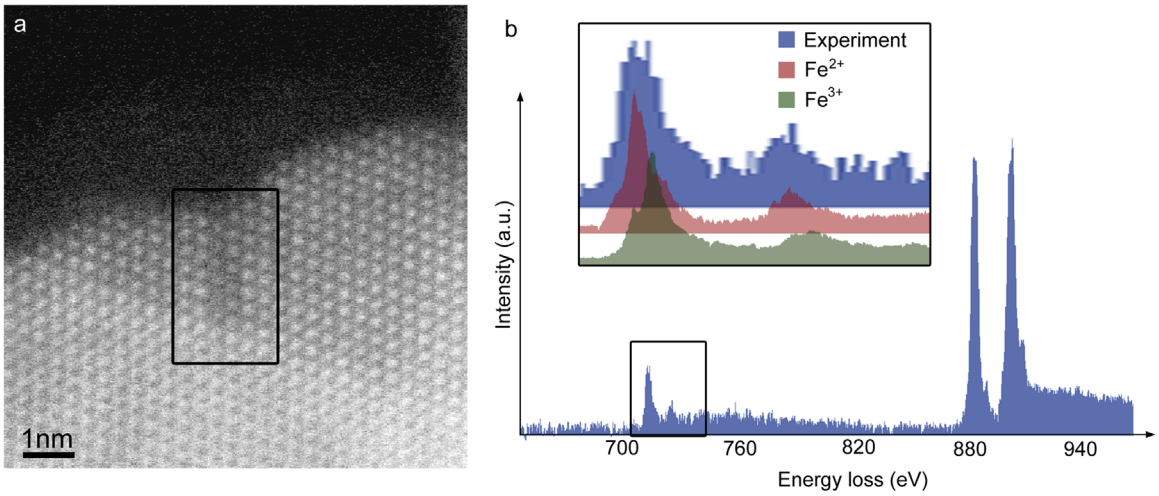

Fig. 4. High resolution STEM-EELS experiments. The darker region indicates the presence of a void inside the ceria nanocrystal. STEM-EELS measurements indicate an enrichment of the Fe doping around these voids (inset). The fine structure of the Fe $L_{2,3}$ edge indicates that these dopants are present as Fe^{2+}.

signal with the fast scanned HAADF-STEM images which were assumed to be free of drift distortions. The energy offset in each projected datacube was calculated using the maximum of the summed Ce M_5 edge as a reference. Next, the HAADF-STEM tilt series, acquired simultaneously with the EELS data, was aligned using cross correlation. These alignment parameters were then applied to all different energy losses of the EELS data cubes providing the set of tilt series $\{\boldsymbol{p}^{(1)}, \boldsymbol{p}^{(2)},\ldots,\boldsymbol{p}^{(l)}\}$ that were used as an input for the direct spectroscopic tomographic reconstruction. During the reconstruction, reference spectra for Fe^{2+}, Fe^{3+}, Ce^{3+} and Ce^{4+} were fitted to the data by incorporating the reference spectra in the tomographic projection matrix. These reference spectra are acquired from CeO_2, CeF_3, ilmenite ($FeTiO_3$) and hematite (Fe_2O_3) samples and are normalized to an integrated intensity that equals one. Normalization is required since the reference spectra are all acquired using different electron doses. However, due to the normalization, thickness information of the reference spectra is lost and it is not straightforward to obtain quantitative information about the concentrations in a given voxel. Quantitative information could be obtained when using quantified reference spectra during the reconstruction. In this study, however, we focused on the spatial distribution and valence state of the Fe dopants inside the ceria nanoparticles.

The reconstruction was calculated using a SIRT algorithm with 100 iterations. One of the main advantages of this technique is that the 3D quantification becomes straightforward since the 3D elemental maps are a direct output of the reconstruction approach. Visualizations of the final reconstructions are presented in Fig. 5. This figure shows 3D renderings of both the HAADF-STEM reconstruction and the reconstructions for Fe^{2+}, Fe^{3+}, Ce^{3+} and Ce^{4+}. As observed from Fig. 5c, no significant Fe^{3+} signal can be seen. This was suggested by the 2D spectrum imaging as presented in Fig. 4, but it is now directly determined from the 3D reconstruction in Fig. 5c.

The HAADF-STEM reconstruction indicates that small voids are present inside the nanoparticle. These voids correspond to the regions with lower intensity as observed in the HAADF-STEM projection image presented in Fig. 3a. The difference between Ce and Fe can not be observed because of the relatively large voxel size (0.81 nm) in the reconstruction. Therefore, multiple atoms are present in each reconstructed voxel yielding a small difference in average Z between a voxel containing a Fe dopant and a voxel without a Fe dopant. From the 3D visualizations of the valency states, illustrated in Fig. 5h, it can be observed that the ceria nanoparticles contain a shell in which the Ce atoms are reduced to Ce^{3+}. Slices through the 3D reconstruction indicate that the

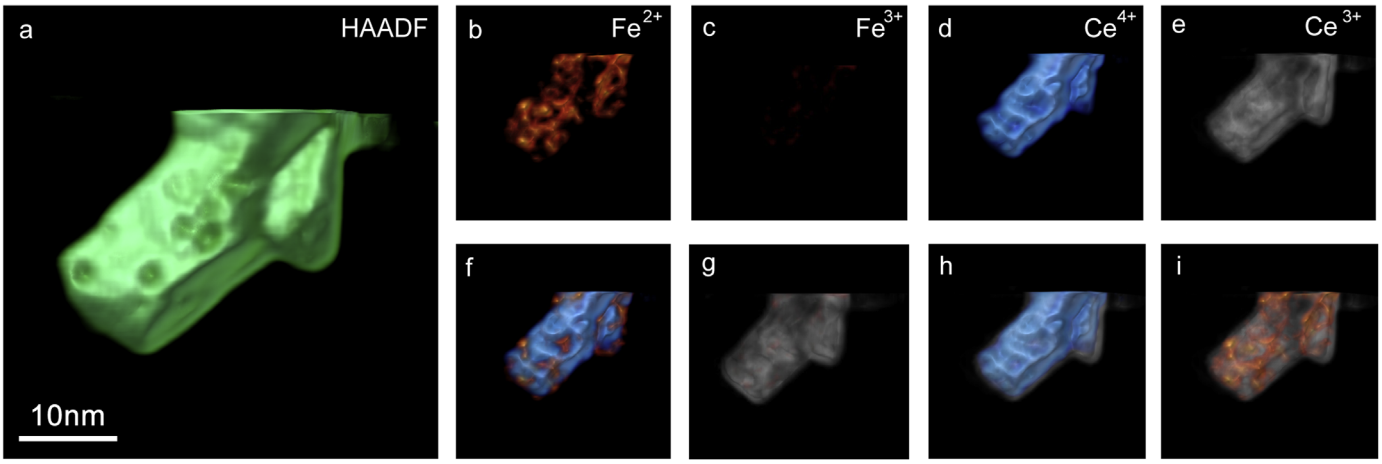

Fig. 5. 3D visualizations of final reconstructions. (a) HAADF-STEM reconstruction showing the morphology of the Fe doped ceria nanoparticle. (b–e) 3D visualizations of the reconstructed Fe^{2+}, Fe^{3+}, Ce^{4+} and Ce^{3+} signal respectively. It can be observed that a negligible Fe^{3+} signal is present in the reconstruction which is in agreement with the 2D STEM-EELS results. (f–i) Overlay of the different 3D visualizations showing the Fe^{2+}-Ce^{4+}, Fe^{3+}-Ce^{3+}, Ce^{4+}-Ce^{3+} and Fe^{2+}-Ce^{3+} reconstructions respectively.

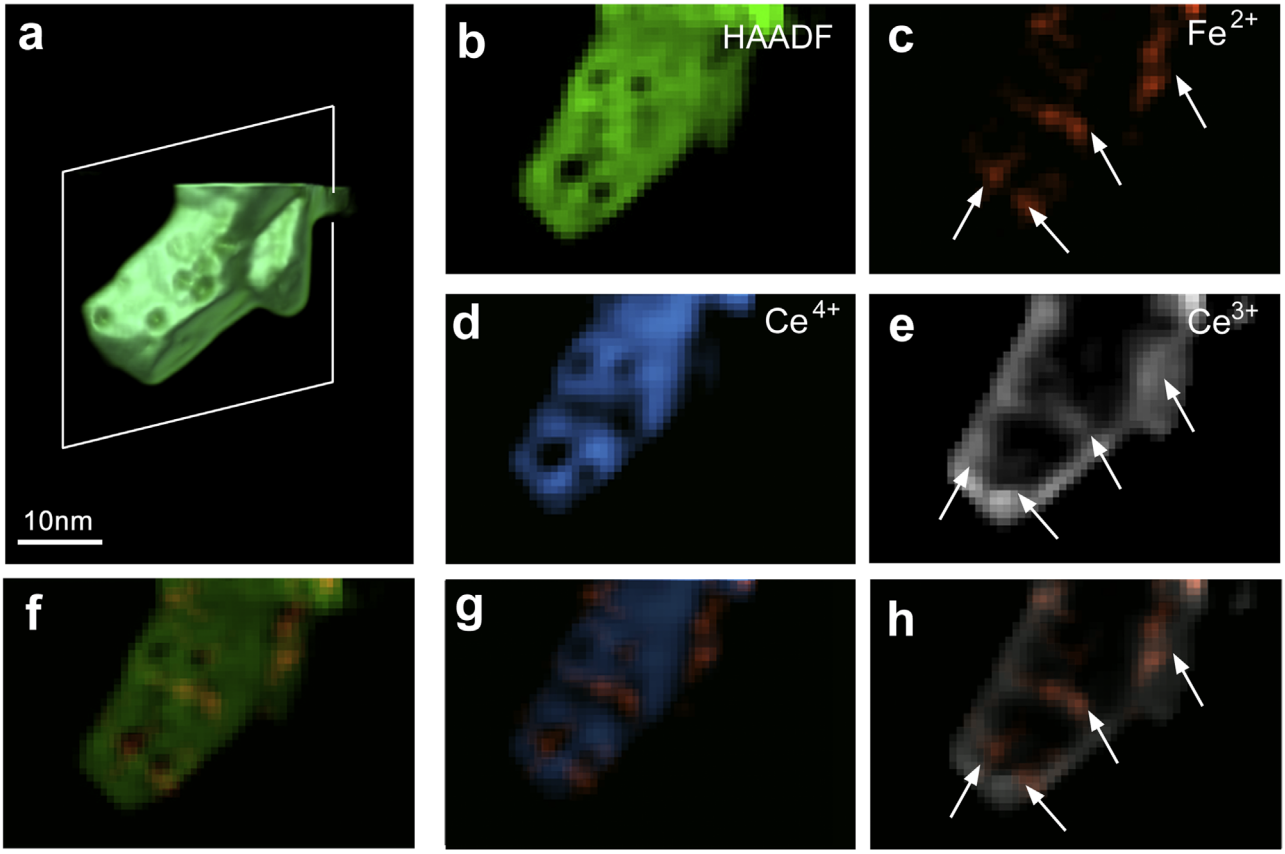

Fig. 6. Slices through the 3D reconstructions. (a) 3D visualization of the HAADF-STEM reconstruction with the representative slice. (b) Slice through the HAADF-STEM reconstruction as indicated in (a). (c–e) Slices through the Fe^{2+}, Ce^{4+}, and Ce^{3+} reconstructions. (f) Overlay of the slice through the HAADF-STEM reconstruction and the Fe^{2+} reconstruction. This indicates that most Fe dopants are present near the voids of the nanoparticle. (g) Overlay of the slices through the Ce^{4+} and the Fe^{2+} reconstruction. (h) Overlay of the slices through the Ce^{3+} and Fe^{2+} reconstructions. As indicated by the white arrows, the presence of Fe^{2+} dopants is often correlated by the reduction of the Ce nanoparticle from Ce^{4+} to Ce^{3+}.

thickness of this shell equals approximately 1.9 nm, which is in agreement with previous studies [3]. In order to investigate the spatial extent of the Fe^{2+} dopants and its correlation to the valency of the Ce nanoparticle, slices through the reconstruction are extracted as presented in Fig. 6.

The white arrows in Fig. 6b, d and h indicate that the presence of the Fe^{2+} dopants is correlated with a reduction of the Ce atoms from Ce^{4+} towards Ce^{3+}. This can also be confirmed from the 3D reconstructions using the different reconstruction methods as presented in Fig. 7. It should be noted that the signal to background ratio of direct spectroscopic electron tomography is improved in comparison to the other 2 methods. In order to quantitatively evaluate the reconstruction quality, the projection error is calculated by simulating the spectrum images using the reference spectra and the experimental tilt values. The sum of the absolute value of the difference between the calculated spectrum images and the experimental ones gives a quantitative measurement for the quality of the reconstruction. The projection error

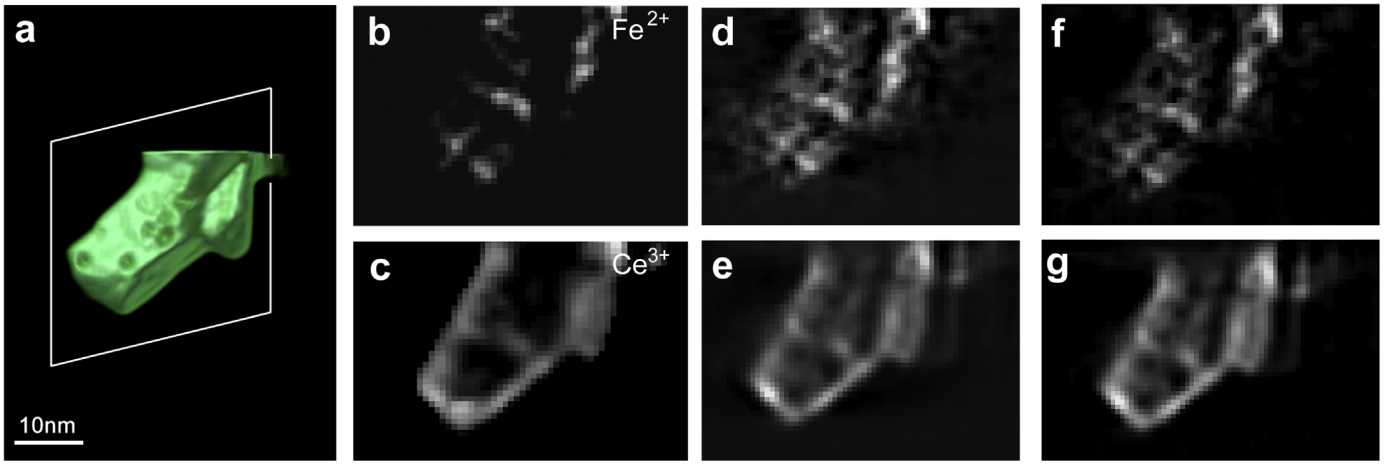

Fig. 7. Comparison between different reconstruction techniques. (a) HAADF-STEM reconstruction indicating the slice through the reconstruction that is presented in figures b–g. (b,c) Slices through the Fe^{2+} and the Ce^{3+} reconstructions obtained using direct spectroscopic electron tomography. (d–g) Corresponding slices from the reconstructions that are obtained using reconstruction methods 1 and 2 as explained in Fig. 1. The grey values in all slices are scaled to the same values.

equals 428.17 for direct spectroscopic electron tomography and 1147.60 and 610.31 for methods 1 and 2 respectively. As an alternative measure, the tilt series was split in two parts which are each reconstructed independently using the three different methods. The correlation between both reconstructions provides a measurement of the quality of the reconstruction. This correlation can be estimated by the ratio of the difference between both reconstructions and the sum of both reconstructions. This value equals 0.22 for direct spectroscopic tomography and 0.25 and 0.28 for methods 1 and 2 respectively. We therefore conclude that both quantitative measurements indicate an improvement of the reconstruction quality for direct spectroscopic electron tomography in comparison to the other methods. The results in Fig. 6 indicate that both ceria as well as the Fe dopants are reduced by the generation of oxygen vacancies. This information cannot be extracted from a single 2D projection image in a straightforward manner because only a small amount of Ce^{3+} is projected simultaneously with a larger amount of Ce^{4+}. In addition, as presented in Fig. 3, the limited SNR hampers the quantification of a single projection image. Moreover, from the comparison of the slices through the HAADF-STEM reconstruction and the Fe^{2+} reconstruction (Fig. 6f), it can be observed that most of the Fe dopants are indeed located near the voids of the nanoparticle.

5. Conclusions

In this work, we have proposed a novel 3D reconstruction technique for spectroscopic data. Using this approach, the prior knowledge of the reference spectra is exploited during the reconstruction process yielding more reliable reconstructions in comparison to conventional techniques, especially for data with a low SNR. The technique is applied to investigate Fe doped ceria nanoparticles. It is revealed that the valency of the Fe dopants corresponds to Fe^{2+} whereas no significant Fe^{3+} signal is detected. In addition, the valency of Ce is investigated showing in a direct manner a correlation between the location of Fe^{2+} dopants and a reduction of the Ce nanoparticle from Ce^{4+} to Ce^{3+}.

Acknowledgments

The work was supported by the Research Foundation Flanders (FWO Vlaanderen) by project funding (G038116N, 3G004613) and by a post-doctoral research grants to B.G. S.B. acknowledges funding from the European Research Council (Starting Grant no. COLOURATOMS 335078). K.J.B. acknowledges funding from The Netherlands Organization for Scientific Research (NWO) (program 639.072.005.). We would like to thank Dr. Hilde Poelman, Dr. Vladimir Galvita and Prof. Dr. Guy B. Marin for the synthesis of the investigated sample.

References

[1] P.A. Midgley, R.E. Dunin-Borkowski, Electron tomography and holography in materials science, Nat. Mater. 8 (2009) 271–280.
[2] P.A. Midgley, M. Weyland, J.M. Thomas, B.F.G. Johnson, Z-contrast tomography: a technique in three-dimensional nanostructural analysis based on Rutherford scattering, Chem. Commun. (2001) 907–908.
[3] B. Goris, S. Turner, S. Bals, G. Van Tendeloo, Three-dimensional valency mapping in ceria nanocrystals, ACS Nano 8 (2014) 10878–10884.
[4] K. Jarausch, P. Thomas, D.N. Leonard, R. Twesten, C.R. Booth, Four-dimensional stem-eels: enabling nano-scale chemical tomography, Ultramicroscopy 109 (2009) 326–337.
[5] G. Mobus, R.C. Doole, B.J. Inkson, Spectroscopic electron tomography, Ultramicroscopy 96 (2003) 433–451.
[6] G. Mobus, B.J. Inkson, Three-dimensional reconstruction of buried nanoparticles by element-sensitive tomography based on inelastically scattered electrons, Appl. Phys. Lett. 79 (2001) 1369–1371.
[7] O. Nicoletti, F. de la Pena, R.K. Leary, D.J. Holland, C. Ducati, P.A. Midgley, Three-dimensional imaging of localized surface plasmon resonances of metal nanoparticles, Nature 502 (2013), 80 ±.
[8] L. Yedra, A. Eljarrat, R. Arenal, E. Pellicer, M. Cabo, A. Lopez-Ortega, M. Estrader, J. Sort, M.D. Baro, S. Estrade, F. Peiro, Eel spectroscopic tomography: towards a new dimension in nanomaterials analysis, Ultramicroscopy 122 (2012) 12–18.
[9] M. Bosman, M. Watanabe, D.T.L. Alexander, V.J. Keast, Mapping chemical and bonding information using multivariate analysis of electron energy-loss spectrum images, Ultramicroscopy 106 (2006) 1024–1032.
[10] T. Yamazaki, Y. Kotaka, Y. Kataoka, Analysis of eel spectrum of low-loss region using the C-S-corrected stem-eels method and multivariate analysis, Ultramicroscopy 111 (2011) 303–308.
[11] J. Verbeeck, S. Van Aert, Model based quantification of eels spectra, Ultramicroscopy 101 (2004) 207–224.
[12] G. Haberfehlner, A. Orthacker, M. Albu, J.H. Li, G. Kothleitner, Nanoscale voxel spectroscopy by simultaneous eels and eds tomography, Nanoscale 6 (2014) 14563–14569.
[13] K.J. Batenburg, S. Bals, J. Sijbers, C. Kubel, P.A. Midgley, J.C. Hernandez, U. Kaiser, E.R. Encina, E.A. Coronado, G. Van Tendeloo, 3d imaging of nanomaterials by discrete tomography, Ultramicroscopy 109 (2009) 730–740.
[14] B. Goris, W. Van den Broek, K.J. Batenburg, H.H. Mezerji, S. Bals, Electron tomography based on a total variation minimization reconstruction technique, Ultramicroscopy 113 (2012) 120–130.
[15] R. Leary, Z. Saghi, P.A. Midgley, D.J. Holland, Compressed sensing electron tomography, Ultramicroscopy 131 (2013) 70–91.
[16] V.V. Galvita, H. Poelman, V. Bliznuk, C. Detavernier, G.B. Marin, Ceo2-modified Fe2o3 for Co2 utilization via chemical looping, Ind. Eng. Chem. Res. 52 (2013) 8416–8426.
[17] M. Meledina, S. Turner, V.V. Galvita, H. Poelman, G.B. Marin, G. Van Tendeloo, Local environment of Fe dopants in nanoscale Fe:Ceo2-X oxygen storage material, Nanoscale 7 (2015) 3196–3204.

[18] P. Gilbert, Iterative methods for 3-dimensional reconstruction of an object from projections, J. Theor. Biol. 36 (1972), 105-&.
[19] F. Bleichrodt, T. van Leeuwen, W.J. Palenstijn, W. Van Aaerle, J. Sijbers, K. J. Batenburg, Easy implementation of advanced tomography algorithms using the astra toolbox with spot operators, Numer. Algorithms 71 (2015) 673–697.
[20] W.J. Palenstijn, K.J. Batenburg, J. Sijbers, Performance improvements for iterative electron tomography reconstruction using graphics processing units (Gpus), J. Struct. Biol. 176 (2011) 250–253.
[21] W. van Aarle, W.J. Palenstijn, J. De Beenhouwer, T. Altantzis, S. Bals, K. J. Batenburg, J. Sijbers, The astra toolbox: a platform for advanced algorithm development in electron tomography, Ultramicroscopy 157 (2015) 35–47.
[22] S. Turner, S. Lazar, B. Freitag, R. Egoavil, J. Verbeeck, S. Put, Y. Strauven, G. Van Tendeloo, High resolution mapping of surface reduction in ceria nanoparticles, Nanoscale 3 (2011) 3385–3390.